Macromolecules

ARTICLE

pubs.acs.org/Macromolecules

Plastic Deformation of Semicrystalline Polyethylene by Molecular Simulation

Sanghun Lee[†] and Gregory C. Rutledge*

Department of Chemical Engineering, Massachusetts Institute of Technology, 77 Massachusetts Avenue, Cambridge, Massachusetts 02139, United States

ABSTRACT: Plastic deformation of semicrystalline polyethylene has been investigated via atomistic Monte Carlo and molecular dynamics simulations. Two deformation modes are considered, both consisting of tensile deformation in the longitudinal direction of the lamellar stack, with either constant lateral dimensions or constant total volume. Stress−strain curves, elastic moduli, yield stresses, and strains are determined at 350 K, with deformation strain rates (in molecular dynamics) ranging from 5×10^6 to 5×10^7 s^{-1}. Fundamentally different yield mechanisms are observed as a function of model constraints, deformation mode, and deformation strain rate. Using Monte Carlo simulations in which the interlamellar noncrystalline material is constrained between two rigid crystalline lamellae, yield stresses in the noncrystalline domain are found to be comparable to those reported previously for amorphous glasses. After yield, in the absence of topological rearrangements of the noncrystalline material, the interphase material hardens postyield with a modulus G_R = 3.36 GPa; in the presence of topological rearrangement, the interphase material flows like a liquid. Using molecular dynamics in which the crystalline domains are thermalized and deformable, tensile deformation with constant total volume is accompanied by changes in the crystal stem orientation that can be attributed to crystallographic slip in the (100)[001] slip system. At the slower strain rate, plastic deformation is accompanied by melting and recrystallization. Meanwhile, for the tensile deformation mode with constant lateral dimensions or for the tensile deformation mode at the faster strain rate with constant total volume, yield apparently occurs with cavitation in the interlamellar domain. Calculated stress−strain curves are constructed by balancing the nonbonded and bonded contributions to stress. The density of entanglements is characterized using Kröger's *Z* algorithm and found to correlate strongly with the fraction of noncrystalline material within the semicrystalline phase.

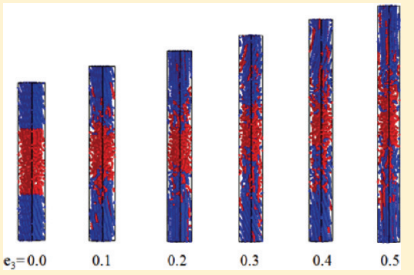

INTRODUCTION

Polymers crystallized in the bulk are almost never completely crystalline due to their long chain nature and the kinetically controlled mechanism of crystallization. Hence, even the most crystallizable polymers exhibit a metastable morphology in the solid state, comprising coexisting crystalline and noncrystalline ("amorphous") domains well below the melting temperature. These "semicrystalline" solids are inhomogeneous in structure, being composed of ordered and disordered phases on the length scale of 1−100 nm. Not surprisingly, their properties are partly attributable to both crystalline and amorphous elements. In addition, a third structural component, an "interphase" with intermediate order, has been proposed, based on theoretical arguments as well as experimental observations.[1−3] In order to understand the behavior of semicrystalline polymer solids, we require a detailed knowledge not only of the individual phases (crystalline, amorphous, and interphase) but also of the interplay among them.

Ever since the seminal realization 50 years ago that the semicrystalline polymer solid state involves crystallites in which the molecular chains necessarily exit and re-enter the crystalline phase through a series of folds and loops,[4−6] numerous experimental studies have characterized the salient features of these materials, such as the thicknesses of the lamellar crystalline and amorphous regions, crystallinity, chain dynamics, etc. Polyethylene is the prototypical semicrystalline polymer solid, for which the largest amount of data is available. An impressive battery of methods, such as differential scanning calorimetry (DSC), pycnometry,[7] Raman spectroscopy,[8,9] solid-state ^{13}C NMR,[10] proton NMR,[11,12] small-angle X-ray scattering (SAXS),[13] small-angle neutron scattering (SANS),[14,15] and scanning electron microscopy (SEM),[16,17] has been used, to name a few. According to these reports, the crystallinity of high-density polyethylene is typically 60−80%, and its lamellar crystal thickness is a few tens of nanometers, depending on the molecular weight of the sample and method of measurement. Keller[4] originally suggested that polyethylene crystal lamellae exhibit regular tightly folded chains that reentry the crystal in an adjacent lattice position, supported by IR, SAXS, and NMR experiments. By contrast, Flory suggested that an irregular reentry model,[18] which subsequently came to be called the "switchboard" model, was required to account for the much more complex behavior of melt-crystallized polyethylene. Yoon and Flory used quantitative calculations and analyses of SANS results to argue for a more-or-less random arrangement of molecular chain exit and re-entry points on the

Received: November 16, 2010
Revised: March 9, 2011
Published: March 28, 2011

surface of the typical melt-crystallized polyethylene lamellar crystallite.[19,20] Using solid-state ^{13}C NMR, Schmidt-Rohr and Spiess[21] quantified the molecular diffusion of methylene groups from the crystalline to amorphous domains in semicrystalline polyethylene and argued that this diffusion is characteristic of a crystal-phase α_c-process (so-called because it takes place at a temperature that exceeds the α-process associated with vitrification). They attributed this process to the diffusion of conformational defects along the chain stem, in accord with models proposed earlier by Reneker and Mazur[22] and by Boyd.[23]

In addition to its morphology in the undeformed state, the plastic deformation of semicrystalline polyethylene has also been extensively studied for decades. During plastic deformation, significant changes occur in both the crystalline and noncrystalline regions. The characteristic features of the crystalline phase are readily observed by well-established techniques such as X-ray crystallography; as a result, the behavior of the crystalline phase under large strain deformation has been the main focus of attention, while relatively little is known about the behavior of the noncrystalline component under these conditions. The dominant mode of plastic deformation in the crystalline phase of polyethylene is crystallographic slip. The crystallographic slip is characterized by the slip plane, with Miller indices (hkl), and the slip direction, with Miller indices $[uvw]$. Several experimental investigations have observed the prevalence of the $(100)[001]$ and $(010)[001]$ slip systems in polyethylene.[24−27] Mechanical twinning and martensitic transformation are also important mechanisms because they can potentially produce plastic deformation even when slip is geometrically unfavorable.[28] Frank et al. first recognized that twinning can play a role during deformation.[29] Bevis et al.[30] and Allan et al.[31] found that $\{310\}$ and $\{110\}$ types are the only twinning modes to be activated during plastic deformation in polyethylene. Solid-state martensitic transformations from orthorhombic to monoclinic crystal structure under shear have been reported based on X-ray[27,32,33] and electron[30,31,34] diffraction experiments. For further information on experimental and theoretical studies of plastic deformation in the crystalline phase of polyethylene, the reader is directed to the review by Galeski.[35]

Meanwhile, consideration of the noncrystalline domain of semicrystalline polyethylene has generally been reduced to a description of the topological connections, in terms of tie chains that have stems in two or more crystalline lamellae ("bridges") and entanglements that occur between neighboring crystalline lamellae.[36] However, direct measurement of entanglements or populations of bridge chains is not easy, especially during deformation. Hence, there have not been many experimental studies that deal specifically with the amorphous or interlamellar domains in semicrystalline polyethylene undergoing plastic deformation. Recently, Bartczak produced samples of semicrystalline polyethylene having different entanglement densities in the amorphous region by controlling the crystallization conditions (i.e., crystallization at high pressure and melt-annealing followed by quenching); his results indicate that elastic deformation is invariant with the entanglement density but that the amorphous domain exhibits rubber-like elastic recovery and permanent plastic flow that does depend on the entanglement density.[37] By contrast, it is often assumed that the number of entanglements is preserved during crystallization, being rejected from the crystal lamellae as "defects" during the crystal growth process; in this case, the density of entanglements in the noncrystalline regions of the semicrystalline state would be higher than that in the melt state. Using an equation that relates the plateau shear modulus in the melt state to the entanglement density, Cheng et al. argued that the higher density of entanglements in the amorphous domain of semicrystalline polyethylene is responsible for the stronger strain-hardening effect.[38]

Relying only on experimental studies, it is difficult to resolve these contrasting viewpoints and to develop a deeper understanding of the plastic response of semicrystalline polymers at the molecular level. For this purpose, molecular simulation is a very useful technique that has enjoyed considerable success in recent years. Over the past decade or so, we have developed an interphase Monte Carlo (IMC) molecular simulation methodology that correctly captures the metastable nature of the semicrystalline solid state in polymers. Beginning with the first report by Balijepalli,[39] metastability was defined explicitly in terms of the competing constraints of molecular connectivity to an ordered (crystalline) phase and an intermolecular packing density within the interlamellar (noncrystalline or amorphous) domain that is incompatible with this ordered phase; the statistical mechanics of this metastability condition have been described previously.[40,41] Interfacial structure, density, energy, and thermomechanical properties have been analyzed in some detail,[39−45] and the method has been extended to isotactic polypropylene as well.[46] In all of these prior works, the crystalline domain was treated as a static component that serves to constrain the interlamellar noncrystalline domain and cannot deform or melt. Such a static treatment was justified based on an assumption of mechanical equilibrium between crystallites and recognition of the very long time scales required to reorganize the entire semicrystalline morphology, compared to local atomic rearrangements made possible by the α_c-process. In this work, we begin to look at large strain plastic deformation, during which the displacement of crystal phase chain segments is expected to be significant. This new model, in which both crystalline and amorphous components are fully thermalized and deformable, is distinguished from earlier work as the semicrystalline model (SM). Initial configurations for the SM model are generated by the IMC methodology, which ensures proper treatment of chain connectivity and packing density in the semicrystalline solid. It is noteworthy in the context of plastic deformation that the IMC model predicts a distribution of loop segment lengths that is characterized by a preponderance of short loops with preferred folding directions but also has a long tail that decays exponentially with segment length.[40,45] We employ both IMC and molecular dynamics (MD) respectively to explore the temporal evolution of the noncrystalline domain alone and the combined noncrystalline/crystalline system under the imposition of large strains.

MODEL AND SIMULATION METHOD

1. Setup and Deformation of the Interphase Model by Monte Carlo. The model employed in this work is the same as that used in the past studies of semicrystalline polyethylene.[39−45] Further details can be found in those works. Briefly, we used the united atom (UA) force field for polyethylene originally developed by Paul et al.,[47] as subsequently modified by Bolton et al.[48] and in 't Veld et al.[43] This force field has been shown to describe accurately both the structure and dynamics of amorphous polyethylene melts as well as the equilibrium melting temperature of *n*-octane[49] and the kinetics of crystal growth for *n*-alkanes.[50,51] The system was composed of 30 chain segments,

each having 100 united atom methylene groups (or methyl, at chain ends), initially placed on a crystal lattice of 3 × 5 × 50 unit cells. The unit cell structure was orthorhombic, with a = 0.771 698 nm, b = 0.444 512 nm, and c = 0.252 678 nm, and there were two chains of two methylene groups each per unit cell. These lattice parameters were adjusted to ensure stresses in the crystal phase corresponding to atmospheric pressure at T = 350 K with the force fields we employed, as described previously by Hütter et al.[44] The resulting crystal phase exhibits pseudohexagonal symmetry in the ab-plane, typical of UA models of polyethylene. The chain stems in the crystal phase were oriented with the {201} plane normal to the z-direction, in anticipation of the low-energy lamellar−amorphous interphase associated with this orientation.[40,52] The resulting orthorhombic simulation box dimension was 2.772 × 2.223 × 12.634 nm^3. In accordance with previous studies, we immobilized the first and last ten UA groups in their crystalline lattice positions. Six chains were selected at random and cut to remove a total of 444 UA groups from the system and arrive at an interlamellar density of ∼0.8 g/cm^3. This procedure resulted in a configuration with 24 bridge segments and 12 tail segments in the interlameller domain. Using periodic boundary conditions in all three directions, this configuration was then simulated at T = 10 000 K for 20 000−40 000 MC cycles (1 MC cycle = 1956 MC moves, corresponding to the number of mobile UA groups in the simulation) in the canonical (constant N, V, and T) ensemble, followed by gradual cooling to 350 K at a rate of 0.241 K per cycle for 40 000 MC cycles. For good statistics, we simulated 18 independent initial configurations taken from the equilibration at 10 000 K. During this MC equilibration step, the MC move set included both local displacement moves (single-site displacement, SS; end-rotation, ER; and rebridging, RB) and global, connectivity-altering moves (reptation, REP; end-bridging, EB), in the proportions of 51:14:14:7:14 (SS:ER:RB:REP:EB), as explained previously.[45] The end-bridging move converts bridge−tail pairs to tail−loop pairs, and vice versa, thereby ensuring a collection of initial structures sampled from an ensemble in which the number and lengths of bridges and loops are equilibrated. Atoms in the noncrystalline interlamellar domain are mobile throughout the MC simulation whereas those in the crystalline domain are fixed. The cutoff radius for the van der Waals interaction was 0.9 nm. Long-range corrections to the pressure and the corresponding virials were used in all calculations. Through slight adjustments of the z-dimension of the interlamellar domain, internal thermodynamic stresses were obtained in accordance with atmospheric pressure of 0.1 MPa at 350 K. The dimensions of the simulation cell after these steps of equilibration were 2.77 × 2.22 × 8.91 nm^3 (Figure 1a).

Beginning with 18 independent initial configurations of the interlamellar domain drawn from the equilibrium distribution, we performed tensile deformation using the IMC method. During deformation, the lateral (x- and y-) dimensions were held fixed, corresponding to a case of pure uniaxial extension ($\lambda_z > 1$, $\lambda_x = \lambda_y = 1$). At every MC cycle, the simulation cell was elongated by the ratio $\lambda_z = 1 + \delta\varepsilon$, where $\delta\varepsilon = 10^{-5}$ is the true strain, so that the dimensions l_x, l_y, and l_z of the simulation cell were determined by eq 1:

$$l_i(t + \Delta t) = \lambda_i l_i(t), \quad l_i(0) = l_{i,0}, \quad i = x, y, z \qquad (1)$$

In general, however, results are reported as a function of engineering strain, and Voigt notation is used for both stresses and strains:

$$e_i(t) = [l_i(t) - l_i(0)]/l_i(0), \quad i = 1, 2, 3 \qquad (2)$$

Using this algorithm, the engineering strain increases exponentially with time. The total number of MC cycles was 44 000; thus, the final cell dimension was 1.55 $l_{z,0}$.

Using the full Monte Carlo move set during deformation (both local displacment and global, connectivity-altering moves), all points in the phase space of the metastable system at a given state of strain are accessible. When only local moves are employed, in addition the initial topology (i.e., number and lengths of loops, bridges, and tails) is preserved within a single simulation; that is, the topological order is "quenched" for the duration of deformation. By averaging over several samples with different topologies, drawn from a simulation with the full move set, the full ensemble of topologies is sampled. This amounts to "turning off" the dynamics responsible for reordering topology on the time scale of deformation, but not overall for the ensemble as a whole.

In general, there exists only a crude correspondence between time and the number of Monte Carlo moves in a Monte Carlo simulation. When only local moves are employed, the system evolves in a manner that is similar to that observed in a molecular dynamics simulation. However, such a Monte Carlo simulation is generally less efficient than MD; thus, only a few MC studies[53−55] have been reported that describe deformation of amorphous glassy polyethylene. In those works, the authors estimated the strain rates associated with local moves to be on the order of 10^8−10^9 s^{-1}. With the introduction of global, connectivity-altering moves such as reptation and end-bridging, the effects of certain longer time scale processes, such as reptation and the α_c-relaxation, become accessible. This can be important, since such processes are certainly active within the experimental time scale. In this work, we performed deformations using the IMC method both with and without such global, connectivity-altering moves (which we denote "slow" and "fast" deformations, respectively). While not precisely quantified, the "slow" deformation rate of strain in this case is certainly very much slower than any deformation rate currently practical by MD simulation.

2. Setup and Deformation of the Semicrystalline Model with Molecular Dynamics. The IMC method described above is expected to render accurately those processes that occur exclusively within the noncrystalline domains. However, during the large strains that give rise to plastic deformation in polyethylene, significant deformation of the crystal phase is also known to occur. Moreover, recent advancement of computing power enables us to access relatively slow deformation rates (∼10^6 s^{-1}) by MD simulation standards. Hence, we performed MD simulations including the entire crystalline and noncrystalline domains. To do this, a set of 18 initial configurations generated by the IMC method were prepared by adding 102 UA sites (51 at each end) per chain in the crystalline domain, for a total of 5616 UA groups in the simulation and a total cell length of 21.630 ± 0.019 nm in the z-dimension. This corresponds to a crystallinity of ∼65%. With a total of 12 chain ends and 5616 atoms, the number-average molecular weight (M_n) is about 13 100 g/mol (936 UA groups) (Figure 1b). The molecular weight distribution constructed in this manner was polydisperse with an average polydispersity index of 1.62. Using periodic boundary conditions in all three dimensions, we have a semicrystalline solid model comprised of crystal lamellae and interlamellar domains that form a 1-D alternating stack in the longitudinal (z) direction and

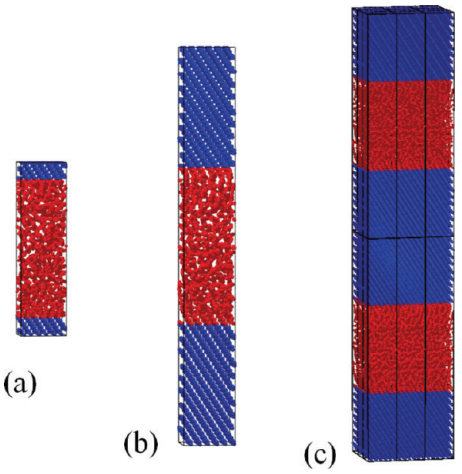

Figure 1. Illustration of the stages of construction for the semicrystalline polymer molecular model. The crystalline domains are evident by the regularity of packing of the chain stems and are shown in blue; the remainder is noncrystalline, comprising both amorphous and interphase components, and is shown in red. (a) First stage: equilibration of the noncrystalline component using the IMC methodology with static crystalline sites. (b) Second stage: augmentation of crystal stems at either end. (c) Third stage: equilibration of the entire semicrystalline model, including both crystalline and noncrystalline sites, at T = 350 K and P = 0.1 MPa. Eighteen of the periodic images are shown for clarity.

are infinite in the lateral directions. This nanocomposite model was then simulated for 8 ns by MD at constant temperature and pressure. We used the Martyna–Tuckerman–Klein thermostat and barostat[56,57] to maintain the temperature at 350 K and the pressure at 0.1 MPa. The cutoff radius and long-range correction were performed in the same manner as for the IMC simulations. The stress tensor was calculated using the Irving–Kirkwood equation,[58] as described by Varnik et al.[59] The reference system propagator was used as the integrator.[60] In this multiple time step scheme,[61] the time step was set to 2 fs for nonbonded interactions and 0.5 fs for stretching, bending, and torsion interactions, respectively. Figure 1 illustrates the basic stages in which the semicrystalline polymer model was constructed in this work.

From the initially undeformed semicrystalline solid configurations obtained by equilibration using MD, tensile deformation was imposed in the z-direction. In the lateral directions, two cases were considered. In the first case, the lateral (x- and y-) dimensions were held fixed, corresponding to a case of pure uniaxial extension ($\lambda_z > 1, \lambda_x = \lambda_y = 1$), similar to that used in the IMC method. In the second case, the lateral dimensions were simultaneously compressed by equal amounts, so as to maintain constant volume in the NVT ensemble ($\lambda_z > 1, \lambda_x = \lambda_y = \lambda_z^{-1/2}$). By adjusting λ_i, the rate of deformation can be controlled, according to eq 1. For MD, $\lambda_z = 1 + \delta\varepsilon$, with $\delta\varepsilon$ taking values of 10^{-7} or 10^{-8}; for a time step of 2 fs, this corresponds to constant true strain rates of 5×10^7 or 5×10^6 s^{-1}, respectively. Henceforth, we refer to these as "fast" and "slow" deformations in the MD part, respectively. Of course, both of these strain rates are quite large compared to typical experimental conditions, a well-known limitation of the MD method; however, it is worth noting that these rates are 1–2 orders of magnitude slower than is typical of recent MD studies of polymer deformation at this level of detail.

Additionally, there are two points to be made regarding the comparison of these simulations to experiments. First, simulations in the $N\sigma_1\sigma_2 l_3 T$ ensemble, where l_3 is the length of simulation box in the direction of imposed strain (z-direction) and σ_1 and σ_2 are the resultant normal stresses in the lateral (x- and y-) directions, would arguably be more representative of the typical experiment; such simulated deformations have been reported previously for glassy amorphous polyethylene, for example.[62,63] However, in the case of semicrystalline polyethylene, the rigidity of the lamellar crystals serves to oppose lateral contraction strongly, so that the simpler case of fixed lateral dimensions is believed to be a reasonably accurate representation of the experimental situation. As shown below, this mode of deformation leads to cavitation and the formation of "microvoids" at relatively modest tensile strain, especially with the relatively fast deformation rates achievable by MD simulation. Such cavitation is also commonly observed in tensile deformation of semicrystalline polyethylene[64] and often leads to complications in the interpretation of plastic behavior. The constant volume deformation mode was employed in an effort to avoid such cavitation. Indeed, in a few experimental SAXS and SANS studies, care has been taken to impose deformation at constant volume in order to prevent the formation of voids that interfere with the scattering measurements.[65,66] The constant volume simulations require the simultaneous application of extension and compression along orthogonal axes and thus bear some resemblance to experiments on plastic deformation of PE conducted in plane strain compression.[24]

Second, the morphology of the samples used in most experiments is spherulitic; in such materials, representative volume elements comprising 1-D layered stacks of alternating crystal and noncrystalline domains, such as that described by the SM here, are generally distributed over a range of orientations with respect to the imposed macroscopic mode of deformation. In such cases, many different deformation modes are realized microscopically in even the simplest experiment, depending on the orientation of each stack relative to the laboratory axes of deformation. Hence, these simulations describe just one of the many possible (microscopic) deformation modes that must ultimately be considered. The results presented here may be regarded as a first step in this direction.

3. Orientation Analysis. The second Legendre polynomial coefficient, $P_2 = [3\langle\cos^2\theta_{ij}\rangle - 1]/2$, is widely used to characterize orientational ordering in nematic systems. Here, θ_{ij} is the angle formed by the chords that join the UA sites bonded to sites i and j, respectively. Using this function, convolved with a square wave function of width 0.4 nm, as described by Ko et al.,[51] local order parameter profiles $P_2(z,e_3)$ were constructed as functions of position, z, and engineering strain, e_3, with resolutions of 0.4 nm and 0.000 50 (initial) to 0.000 75 (final), respectively. To quantify the volume fraction crystallinity, the same order parameter was convolved in all three directions, with a spatial resolution of 0.4 nm in each direction. The crystallinity was then calculated by counting the number of points with $P_2(r) > 0.6$ and dividing by the total number of points. The choices of the function $P_2(r)$ as the crystal phase order parameter and the cutoff of 0.6 are both somewhat subjective; this particular combination has been compared to alternative choices in previous studies of crystal growth kinetics and found to provide a good measure of crystallinity.[50]

4. Topological Analysis. Entanglements within the amorphous domain are thought to be important to mechanical properties of semicrystalline polymers at large strain. Loops belonging to different crystal lamellae that are topologically constrained so that they cannot disentangle from one another are similar mechanically to bridges that run directly from one lamella to the

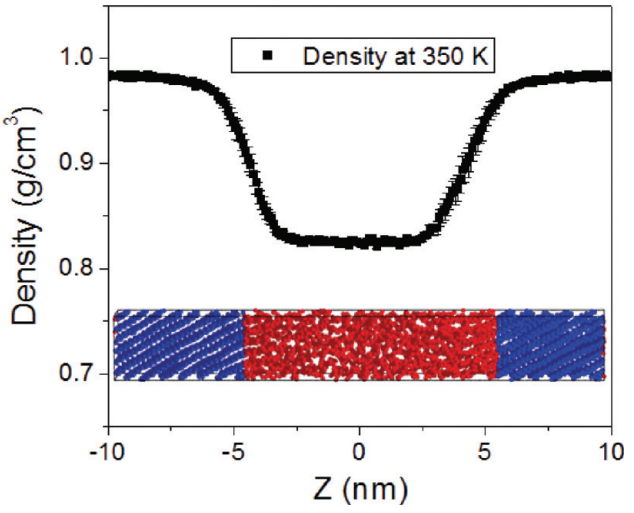

Figure 2. Density profile of semicrystalline polyethylene at 350 K in the undeformed state. A snapshot of the semicrystalline solid model is shown below the data for clarity. The crystalline (blue) and noncrystalline (red) domains are repeated periodically in the z-direction, consistent with the model of semicrystalline polyethylene comprising a 1D stack of crystal, interphase, and amorphous regions.

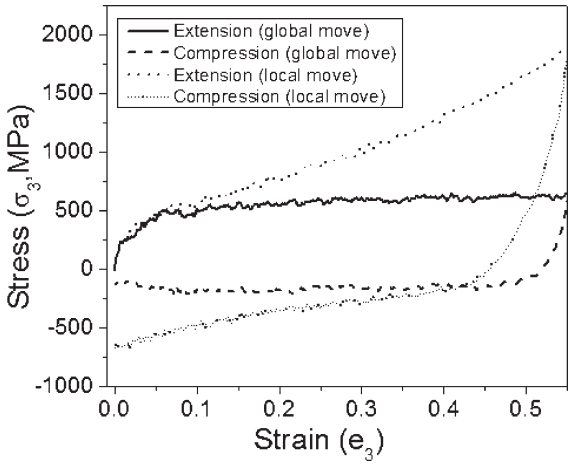

Figure 3. Stress (σ_3)−strain (ε_3) curves obtained by IMC at 350 K. The simulation cell undergoes extension in the z-direction up to a strain of 0.55, and then the strain rate is reversed and the cell returned to its original size.

other. Recently, algorithms to quantify entanglements have been developed, based on the primitive path network;[67−70] the primitive path is defined as the shortest path connecting the two ends of a chain with the same topology as the chain itself. "Kinks" occur where two chains cross one another and result in a point of contact that limits further reduction of the primitive path. Such kinks are topological constraints and have been identified with physical entanglements of the type envisioned to be operative in the rubbery plateau behavior of polymer melts. In their pioneering work on primitive path analysis (PPA), Everaers et al.[67] proposed to define an "entanglement length", N_e, as the number of monomers or sites between topological constraints in the original model representation and an "entanglement density" as the number of topological constraints per unit volume. From the trajectories of an amorphous polymer melt obtained by MD simulations, they showed that the relation $G_N = \rho k_B T/M_e = \rho k_B T/m_0 N_e$ is upheld for various polymer systems. Here, G_N is the plateau shear modulus, ρ is the amorphous melt density, M_e is the molecular weight between entanglements, and m_0 is the monomer molecular weight. Subsequently, the Z/Z1[68,69] and CReTA[70] algorithms have been proposed as alternative methods to extract the primitive path network from a simulation trajectory. Whereas in the PPA contour reduction is achieved through minimization of an elastic energy, the Z/Z1 and CReTA algorithms adopt a geometric approach. Detailed comparisons of the original PPA, Z, and CReTA algorithms have been reported.[69,70] The Z code, which solves the problem of "shortest multiple disconnected path" (minimum total Euclidian length), is computationally more efficient than the CReTA and original PPA methods by 1 and 3 orders of magnitude, respectively. In this work, we use Kröger's Z algorithm[68,69] to characterize the entanglement network of the noncrystalline domain.

RESULTS AND DISCUSSION

1. Molecular Dynamics of the Undeformed Interlamellar Domain. Here we report the first molecular dynamic simulations of the interlamellar domain of the prototypical semicrystalline polymer, polyethylene, complete with excluded volume and intramolecular connectivity to the neighboring lamellar crystallites. Eighteen independent initial configurations of the interlamellar domain, with the {201}-oriented crystal−amorphous interface, were generated by IMC as described above and subsequently simulated for 8 ns of NPT molecular dynamics at 350 K, prior to imposing any deformation. Figure 2 shows the density profile in the direction normal to the crystal−amorphous interface, averaged over the ensemble of 18 structures. The origin of the z-axis corresponds to the center of the amorphous domain. To confirm that the resulting structure is dynamically metastable (i.e., in a state of a local equilibrium, despite the removal of the constraints on crystal registry and system density that were in effect during IMC simulations), the positions of the crystal−amorphous interfaces were monitored using the method of Gibb's dividing interfaces.[44] We confirmed that these interfaces remain in place, at positions of ±4.5 nm, for the 8 ns duration of the simulations, in the absence of deformation. The calculated volume percent crystallinity in the undeformed, metastable state was 58%. The calculated density at the centerline of the interlamellar domain was 0.83 g/cm^3. This value is in very good agreement with the atmospheric pressure simulations of Capaldi et al.[63] for a fully amorphous melt at 350 K as well as the previous IMC results of Hütter et al.[44] The structure, topology and thermodynamic properties of the current system are expected to be similar to those reported previously by Hütter et al.[44] and by in 't Veld et al.;[45] the reader is referred to these earlier reports for further details.

2. Deformation of the Interphase by Monte Carlo. Figure 3 shows stress−strain curves obtained during deformation of the IMC model, in which the crystal lamellae are displaced as rigid bodies. These stresses were computed only for the interlamellar domain material. The "fast" deformation (using only local moves) shows an elastic behavior at very low strain up to yield at a strain of $e_3 = 0.02$, followed by irreversible plastic deformation and strain hardening. After extension of the system to a strain of 0.55, the deformation was reversed, resulting in the rapid relaxation of stress to zero at a strain of about 0.45 and the development of compressive stress thereafter. By contrast, the "slow" deformation (including global, connectivity-altering moves) shows similar

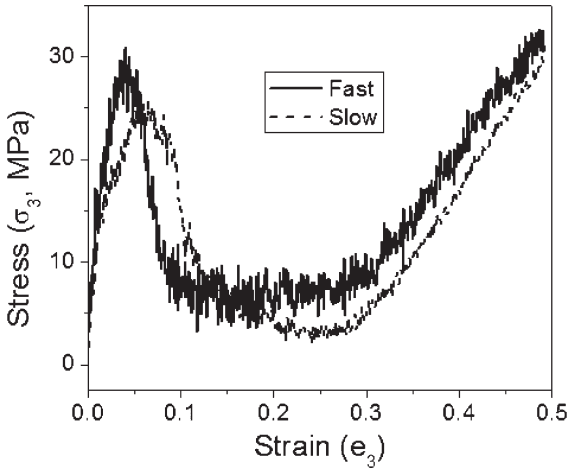

Figure 4. Stress (σ_3)−strain (ε_3) curves of the fast and slow deformations with no lateral strain.

behavior up to the point of yield but exhibits flow without strain hardening thereafter, consistent with a fully equilibrated amorphous domain above its glass transition.

Both "fast" and "slow" deformation simulations using IMC predict a large yield stress of roughly σ_y = 200 MPa. This value is comparable to the yield stress of 200 MPa (at a yield strain of 0.15) obtained by molecular dynamics simulation of a fully amorphous polyethylene glass at 100−200 K, using the same force field[62,63] and somewhat higher than values of 90−170 MPa at 100−200 K reported for Monte Carlo simulations of polyethylene glass deformation by Michels and co-workers.[54,55] It contrasts with a typical yield stress of 10−20 MPa for semicrystalline polyethylene at room temperature.[71]

This large yield stress probably has its origins in two features of the IMC model employed here. First, the connectivity of chains to the rigid crystal boundaries restricts their mobility, analogous to glasses. It has been shown in simulated deformation of glassy polymers that the development of stress up to the point of yield is largely intermolecular in nature.[53−55] Although the global moves employed here, in particular the end-bridging move, permit dramatic, instantaneous changes in the topology of the interphase material, they do not significantly alter the local packing. From the observation that the yield point is relatively insensitive to the inclusion of connectivity-altering Monte Carlo moves, we conclude that yield is indeed a function primarily of the intermolecular packing interactions and that the effective deformation rate is still high, as far as these interactions are concerned. Indeed, the use of $\delta\varepsilon = 10^{-5}$ in this work was chosen to be consistent with previous MC simulations of glassy polyethylene deformation employing local moves only.[54,55] This conclusion is also consistent with the relatively high value of elastic modulus obtained here: C_{33} = 2.2 ± 0.3 GPa at 350 K. This compares with C_{33}= 0.90 GPa at 435 K obtained by in 't Veld et al.,[45] using the same model. However, in 't Veld et al. used a MC deformation protocol involving a step strain of 0.0125 and re-equilibrating for 25 000 MC cycles, while the same strain is reached here in less than 1250 MC cycles. With respect to intramolecular interactions, however, the picture is quite different. These are thought to carry most of the stress beyond the point of yield.[53−55] In the absence of global moves, the interphase material hardens postyield, with a hardening modulus G_R = 3.36 ± 0.023 GPa. This is significantly larger than the G_R = 0.42−1.27 GPa estimated for a glassy polyethylene

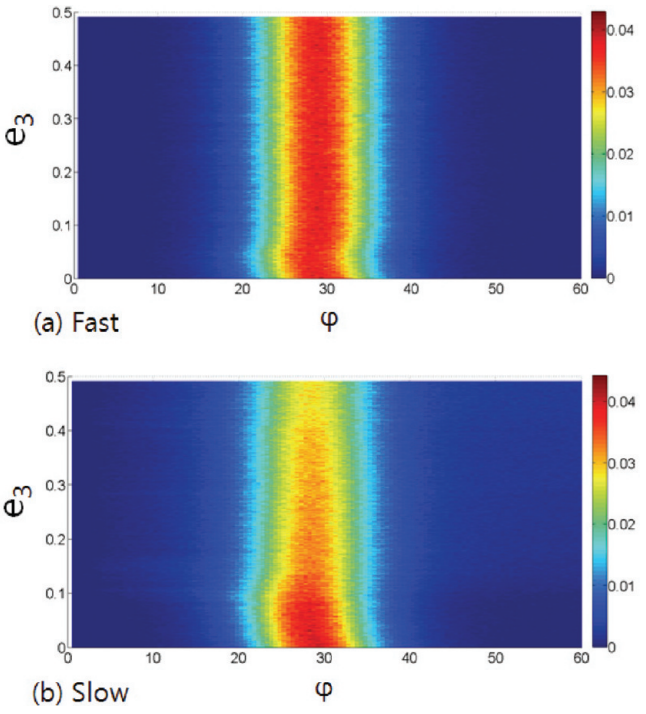

Figure 5. Angular distribution of the chain segment vectors in the crystalline phase during the deformations with fixed lateral dimensions. The orientation angle is measured with respect to the crystal−amorphous interface normal. (a) "Fast" deformation; (b) "slow" deformation.

by Li et al.[54] With the inclusion of global, connectivity-altering moves, such intramoleclar stresses cannot be supported, and the material consequently flows in a liquidlike manner. Comparing the results for the two types of IMC simulations in Figure 3 serves to demonstrate that such topological rearrangements are probably not important at low strain but have a profound effect postyield.

The second and more important feature of the IMC model, with respect to yield, is that it cannot capture processes involving the crystal domains. Comparing the results of the IMC simulations to experiments serves to demonstrate that elastic modulus can be accurately determined with a model that considers deformation of the interlamellar domain only, whereas the yield stress is considerably overestimated. This lack of agreement suggests that the crystal domains are important participants in the experimentally observed yield phenomenon. Both of these shortcomings are addressed next, using molecular dynamics and the full semicrsytalline model (SM), wherein the crystal domains are allowed to deform and melt.

3. Deformation of the Semicrystalline Model by MD. *Deformation with Constant Lateral Dimensions.* First, we consider the case of deformation with constant lateral dimensions (i.e., no lateral strain). Deformations were performed at both "fast" (5×10^7 s^{-1}) and "slow" (5×10^6 s^{-1}) rates of strain. Figure 4 shows the resulting stress (σ_3)−strain (e_3) curves for these cases. During both the "fast" and "slow" deformations, yield occurs at an engineering strain of about e_3 = 0.03, with a yield stress around σ_y = 25−30 MPa, followed by considerable softening. This yield stress is almost an order of magnitude smaller than that observed in the IMC simulations and in good accord with experimental results for bulk cast polyethylene of comparable lamellar thickness (∼10 nm)

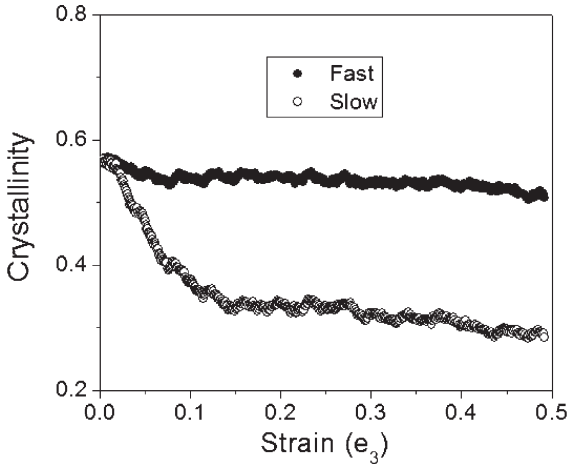

Figure 6. Evolution of crystallinity during the deformations with fixed lateral dimensions.

deformed in tension at 293 K.[72] In both cases, cavitation is observed in snapshots of the simulation between strains of 0.1 and 0.15, which can be attributed to the dilatational nature of this mode of deformation. We speculate that the onset of plastic deformation and cavitation has its origins in the loss of nonbonded contacts between chains, starting around the yield point. Between strains of 0.1 and 0.3, the system "flows", as loops, bridges, and tails disengage and the cavity expands. The strain hardening behavior observed beyond a strain of 0.3 is due to chains being pulled taut between crystallites; such "taut tie" chains would include not only bridges but also entangled loops. Fitting straight lines to the stress−strain data up to $e_3 = 0.015$, we obtain stiffness values by MD of $C_{33} = 0.83 \pm 0.05$ GPa ("fast") and 0.72 ± 0.04 GPa ("slow"), which are very close to that determined previously by in 't Veld et al.[45]

Parts a and b of Figure 5 display the angular distribution of the segment vectors in the crystalline domain (middle 4 nm) for the "fast" and "slow" deformations, respectively. The angles were measured with respect to the crystal−amorphous interface normal (the z-direction). In the undeformed state, the chains in the crystalline phase are tilted by about 30° from the {201} interface normal to minimize interfacial energy.[40,52] These plots show that the angular distribution of chains is hardly altered in either case, for strains up to 0.5. This contrasts with the evolution of angular distributions when volume is conserved; this is discussed later.

Figure 6 shows the change of crystallinity during the deformations with fixed lateral dimensions. The crystallinity observed during the "fast" deformation decreases from 58% to 51% (excluding the volume of the cavity), and that observed during the "slow" deformation drops to 30%. There is no indication of recrystallization, in contrast to that which is observed during volume-conserving deformation.

Deformation with Constant Volume. Next, we describe the results of plastic deformation under the conditions of constant volume, so as to avoid the complications of cavitation that arise under pure extension. Figure 7a shows the stress (σ_3) versus strain (e_3) response for both the "fast" and "slow" deformation strain rates. From these curves, several important mechanical properties can be determined. At low strains ($e_3 < 0.07$), we estimate elastic constants at 350 K of 0.175 ± 0.003 and 0.160 ± 0.005 GPa by the "fast" and "slow" deformations, respectively.

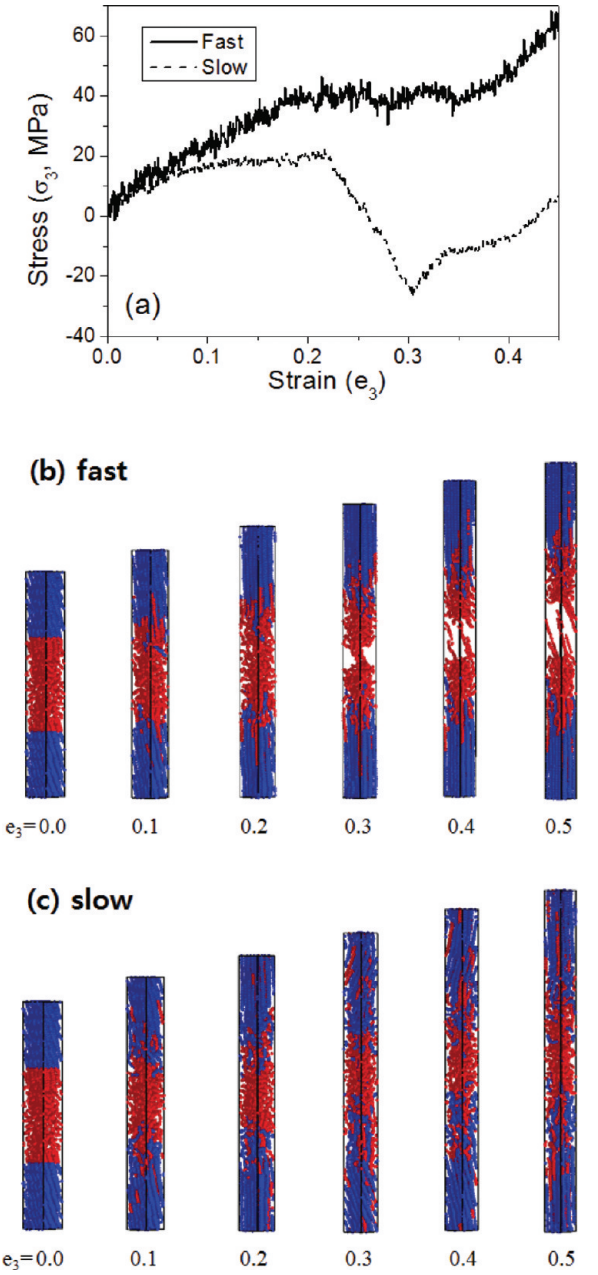

Figure 7. (a) Stress (σ_3) versus strain (e_3) response for volume-conserving tensile deformations at "fast" and "slow" strain rates. (b) Snapshots of a representative simulation undergoing "fast" and (c) "slow" volume-conserving deformations. UA sites that start out in the crystalline domain (in the undeformed state) are colored blue and retain this color throughout the subsequent deformation; all other sites are colored red. This serves to reveal the interchange of sites between the crystalline and noncrystalline domains. It is worth noting that sites can move with facility within and between both the crystalline and noncrystalline domains.

The values are weakly strain rate dependent and are somewhat lower than the previous estimate of $C_{33} = 0.90$ GPa (at 435 K) for the interlamellar domain by in 't Veld et al.[45] This discrepancy can be attributed to Poisson effects, whereby the nonzero lateral strains (in x and y) also contribute a factor of approximately $-(C_{13} + C_{23})e_3^{1/2}$ to the z-component of stress observed here. We have not attempted to resolve further the elastic

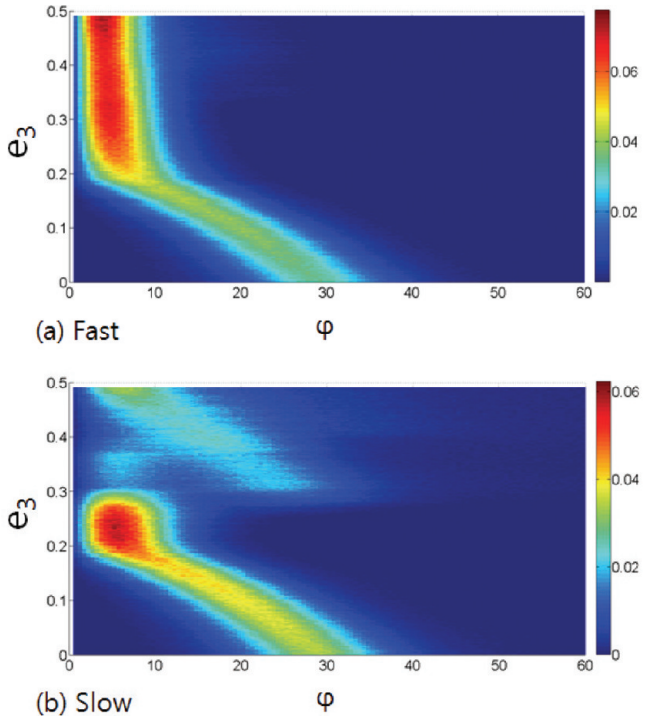

Figure 8. Angular distribution of the chain segment vectors in the crystalline phase during the (a) fast and (b) slow volume-conserving deformations. Orientation is obtained with regard to the crystal—amorphous interface normal.

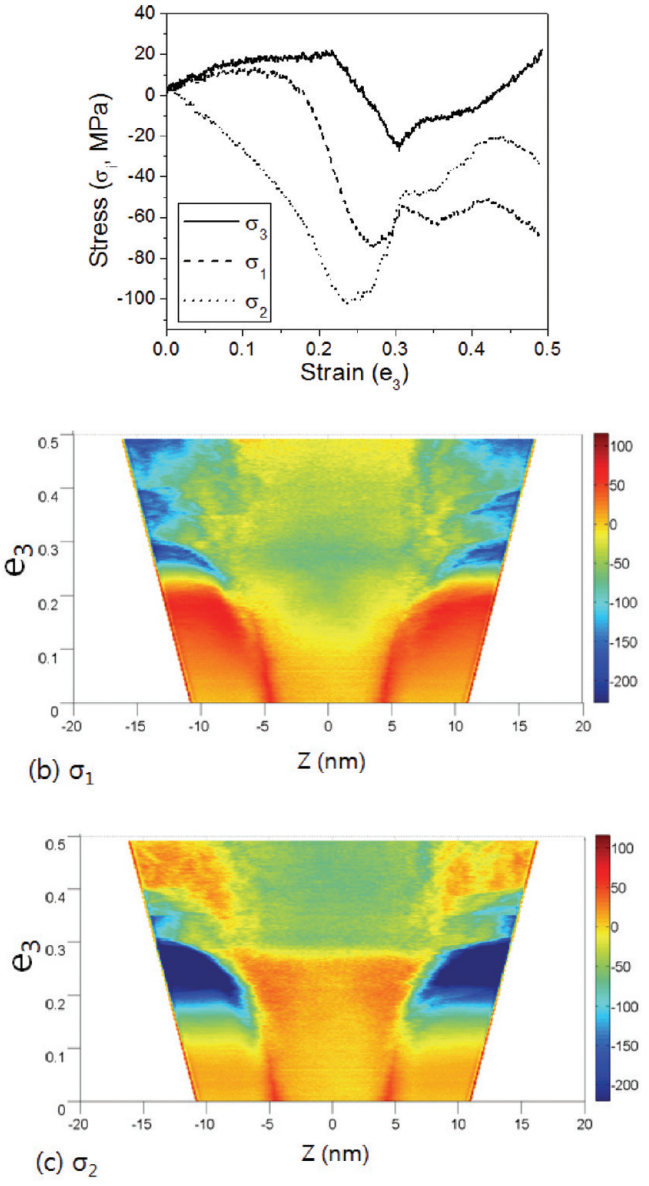

Figure 9. (a) Normal components (σ_3, σ_1, and σ_2) of the total stress tensor versus applied strain (e_3) for volume-conserving deformation at the "slow" strain rate. (b) σ_1 and (c) σ_2 of the slow deformation are shown as a function of both e_3 and z.

constants measured here into their corresponding stiffnesses; for this, the reader is referred to in 't Veld et al.[45] In the case of "fast" deformation, yield is observed at a strain of $e_3 = 0.17$, with a yield stress $\sigma_y = 40$ MPa. After yielding, a plateau in the stress—strain response is observed up to $e_3 = 0.3$. At this point, strain hardening with a modulus $G_R = 0.44 \pm 0.01$ GPa (from strain of 0.35 to 0.5) is observed. In the case of "slow" deformation, yield occurs at $e_3 = 0.07$ with $\sigma_y = 12$ MPa, beyond which a plateau with only modest strain hardening continues up to $e_3 = 0.22$. Snapshots of a typical simulation at several states of strain for both "fast" and "slow" deformations are shown in Figure 7b,c. Examination of the crystal phase shows a change in orientation of the chain stems within the crystal, which rotate toward the direction of applied stress. This is confirmed by a plot of the angular distribution of the segment vectors (in the middle 4 nm) of the crystalline phase with respect to the crystal—amorphous interface normal, shown in parts a and b of Figure 8 for the "fast" and "slow" deformations, respectively. In both cases, the chain segments originally tilted at 30° with respect to the interface normal (indicative of a {201}-oriented lamellar/amorphous interface) become aligned nearly parallel to the interface normal (indicative of a {001}-oriented lamellar/amorphous interface). Such rotation can only be explained by the occurrence of fine crystallographic slip of the (100) plane in the [001] direction. Beyond $e_3 = 0.07$, the responses to "fast" and "slow" deformations diverge. We attribute this divergence to the mobility of defects generated during deformation. Under "slow" deformation conditions, these defects are sufficiently numerous and mobile to accumulate at the crystal—amorphous interphase, resulting in the apparent melting of the crystal phase, as discussed later; under "fast" deformation conditions, melting is not observed, and the stress continues to rise as new defects are generated. By $e_3 = 0.2$, the crystal stems have rotated fully into the direction of applied stress, and this mechanism of response has been exhausted. At this point, the "fast" deformation yields through cavitation, in accord with the earlier simulations deformed at fixed lateral strain. On the contrary, in the "slow" deformation, a dramatic reduction in the z-component of normal stress, σ_3, is observed, even when averaged over the 18 independent simulations; this stress reduction may be traced to a morphological transition in the crystal phase, which is apparent in the snapshots of Figure 7c. The chain stems in the crystal suddenly revert from the {001} interface back to {201} interface, resulting in formation of a crystallographic twin. This reorientation is apparent also in Figure 8b; its rapidity is suggestive of an instability, possibly due to the lower energy of the {201} interface.[40,52] The exact nature of this instability

dx.doi.org/10.1021/ma1026115 |*Macromolecules* 2011, 44, 3096–3108

warrants further investigation but is beyond the scope of this report.

Figure 9a displays all three diagonal components (σ_3, σ_1, and σ_2) of the total stress tensor versus applied strain e_3 during the slow deformation. This semicrystalline system is not only inhomogeneous but also anisotropic; hence, the stresses in the lateral directions, σ_1 and σ_2, show quite dissimilar behavior. For small tensile strain in the z-direction, σ_2 is negative, indicating that the semicrystalline model is under compression in the y-direction, whereas σ_1 is slightly positive, indicating that the cell is under tension in the x-direction. This suggests that, even though the system is compressed in the x- and y-directions at the same rate of strain to ensure constant volume, the cell nevertheless remains in tension in the direction of chain tilt within the crystal phase. In Figure 9b,c, the lateral stress components (σ_1 and σ_2) are shown as functions of both e_3 and z, in order to resolve the crystalline and noncrystalline contributions to the total stress; these lateral stresses develop very differently with strain in the crystalline and noncrystalline domains, consistent with two mechanically nonequivalent domains arranged in parallel and strained equally in both e_1 and e_2. According to the unit cell parameter and the 30° tilt of the chain stems with respect to the {201} interface, the atoms in the crystalline phase are separated by 0.92 nm in the x-direction, whereas they are separated by only 0.44 nm in the y-direction (also, the b-direction of the unit cell). Up to a strain $e_3 = 0.2$, the chains rotate from 30° ({201} orientation) to 0° ({001} orientation), while the separation between chains along the x-direction decreases. Around $e_3 = 0.2$, the chains in the crystal are fully aligned with the applied stress, and the (100)[001] crystallographic slip system has been fully exhausted. At this point, σ_1 changes from tension to compression and begins to track with σ_2. Thus, σ_3 and σ_1 appear to be strongly coupled at low strain, through the mechanism of (100)[001] crystallographic slip. This orientational variation of crystal chains is not observed in the deformation in which lateral dimensions are held constant; some amount of

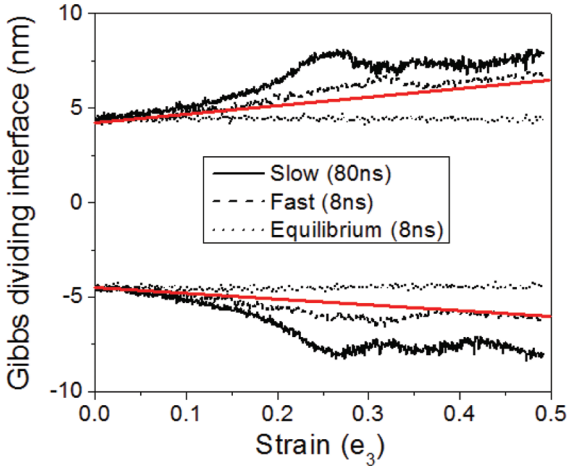

Figure 10. Location of the Gibbs dividing interfaces between crystalline and noncrystalline domains during the "fast" and "slow" deformations at constant volume and in the absence of deformation ("equilibrium"). The locations of the interfaces under the assumption of affine deformation of both crystalline and noncrystalline domains are shown in red.

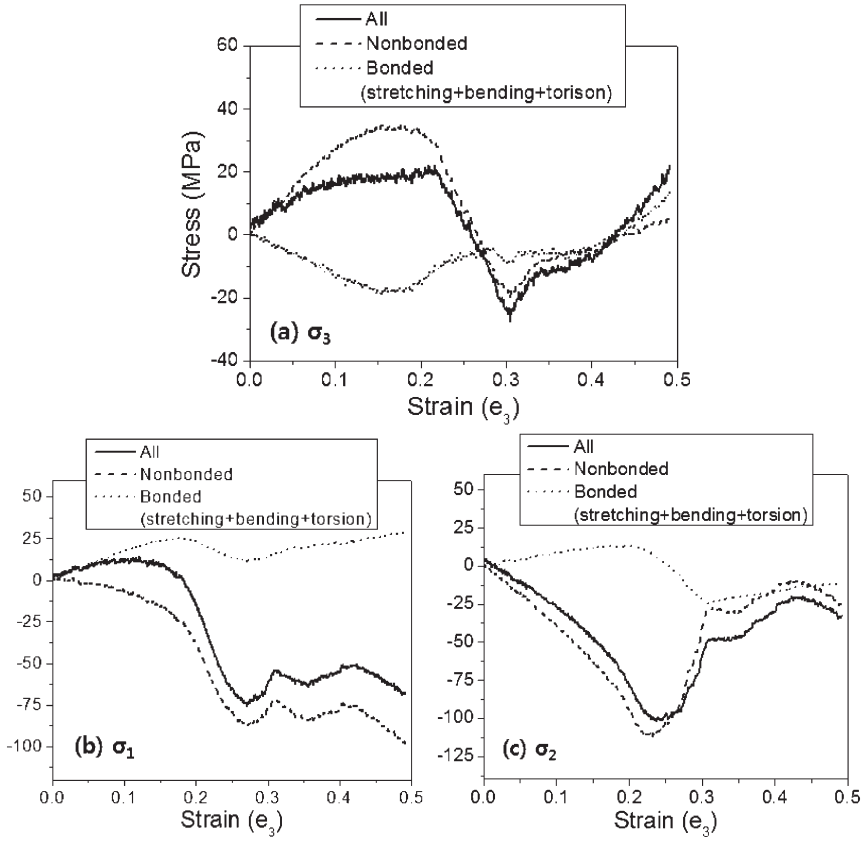

Figure 11. Nonbonded and bonded (i.e., stretching, bending, and torsion) contributions to stresses. (a) σ_3, (b) σ_1, and (c) σ_2. Each component at the undeformed state is offset to 0.

dx.doi.org/10.1021/ma1026115 |*Macromolecules* 2011, 44, 3096–3108

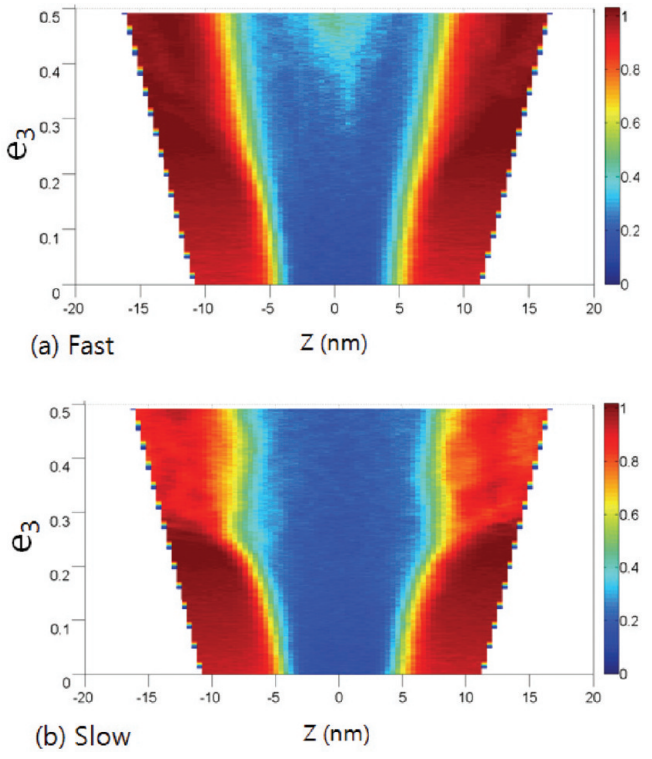

Figure 12. Local order parameter profiles $P_2(z,e_3)$ of the volume-conserving deformations: (a) "fast" deformation; (b) "slow" deformation.

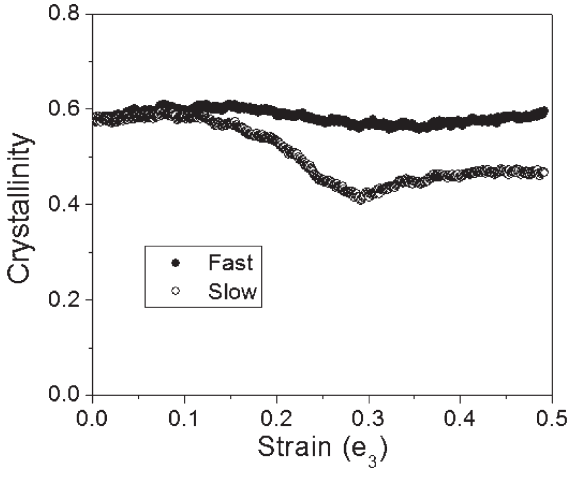

Figure 13. Change of crystallinity during the volume-conserved deformations.

compressive strain in the *x*-direction is necessary to accommodate this response to deformation.

The locations of the crystal amorphous interfaces are calculated by the method of Gibbs dividing surface[44] and plotted as functions of strain for both the "fast" and "slow" deformations in Figure 10. Also shown are the locations of the interfaces that would occur if the deformation were affine, i.e., equal strain e_3 in both crystalline and noncrystalline domains. As is evident from Figure 10, the actual interface displacement is greater than affine, confirming that the contribution to strain from the softer, noncrystalline phase is greater than that from the stiffer, crystalline phase. However, the displacement of the interface may not be due entirely to the difference in mechanical stiffness of the two domains. In addition, melting or crystallization induced by the applied strain may lead to an exchange of material between the two domains, which would also give rise to displacement of the interface. This possibility is thought to be more important for the "slow" deformation than the "fast" deformation and is discussed later.

In Figure 11, the nonbonded (both intramolecular and intermolecular) and bonded (stretching, bending and torsion) contributions to the diagonal stress components are shown. Throughout the entire range of strain, the nonbonded contributions are of the same signs as the total stresses, whereas the bonded components generally oppose the observed stresses. The only exception is σ_3 at the highest strains ($e_3 > 0.4$), where the large tensile stress borne by the bonded forces of the chain is indicative of chains being pulled taut between crystalline lamellae. This behavior of the bonded contribution to stress is somewhat counterintuitive but is consistent with previous observations of deformation in melts and rubbers by Gao and Weiner,[73−75] using nonequilibrium MD simulations. They observed that nonbonded (i.e., excluded volume) interactions are locally anisotropic due to steric shielding associated with bonded portions of the chain and that the net effect of these interactions is to place the bonded portions of the chain in compression at densities typical of the melt. As the material is deformed and made anisotropic, the consequences of this steric shielding and compressive bonded stresses may be observed macroscopically. Gao and Weiner introduced the concept of "intrinsic monomer stresses" to help explain this phenomenon.[73]

In Figure 12, the orientational order parameter profiles $P_2(z,e_3)$ are shown for both "fast" and "slow" deformations. In the "fast" deformation (Figure 12a), there is no significant variation of the orientational order parameter in the crystalline phase; it is consistently high, a characteristic of the crystalline phase. Meanwhile, a slight increase in orientational order in the middle of the amorphous phase is observed for strains larger than $e_3 = 0.3$. This is attributed to the drawing taut of chains (bridges and entangled loops) between two crystallites. In the "slow" deformation, the orientational order in the amorphous phase increases slightly, while that in the crystalline phase also increases slightly (from ∼0.92 to ∼0.99) up to $e_3 = 0.2-0.3$. Beyond $e_3 = 0.3$, the orientational order in the crystal phase decreases rapidly, to about ∼0.88, in concert with reconstruction of the crystalline domain in these simulations to form a crystallographic twin. The formation of the twin apparently allows a certain amount of recrystallization to occur as deformation proceeds beyond $e_3 = 0.3$.

The change in crystallinity with strain during deformation at constant volume can be seen more clearly in Figure 13. No remarkable change is observed during the "fast" deformation over the entire range of strain. By contrast, during the "slow" deformation, crystallinity decreases from 58% to 41% around $e_3 = 0.3$ and then increases slightly to 44% by the end of simulation ($e_3 = 0.5$). This behavior of the "slow" deformation is evidence for a melting−recrystallization phenomenon, originally proposed by Flory and Yoon,[76] as a mechanism for plastic deformation in semicrystalline polymers. As evident in Figure 12b, the melting−recrystallization phenomenon occurs at the interfaces between the crystalline and noncrystalline domains. This mechanism is supported by the SANS measurements of Wu et al.[65] in which a large reduction of scattering intensity at zero angle, $I(0)$, was observed during plastic deformation in the pure shear mode (i.e., elongation in one direction combined with compression in

dx.doi.org/10.1021/ma1026115 |*Macromolecules* 2011, 44, 3096–3108

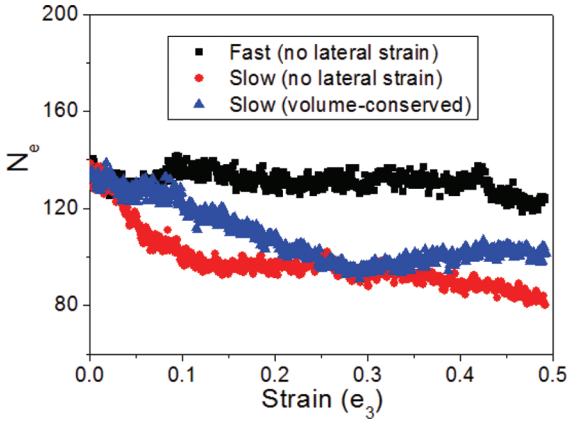

Figure 14. Evolution of N_e during the deformations.

one of the lateral directions). It is worth noting that both crystallographic slip and melting/recrystallization are observed in the "slow" volume-conserving deformation in the range of $0.1 < e_3 < 0.2$ (cf. Figures 8 and 13); we conclude that these two mechanisms are not mutually exclusive, as is often implied, but that crystallographic slip is more important at small strain, giving way to melting/recrystallization at large strain.

In summary, the volume-conserving deformation discussed up to this point has the advantage of eliminating dilatation and associated mechanisms as a source of yield and plasticity. In both "fast" and "slow" deformations, crystallographic slip in the (100)[001] is observed to begin almost immediately with applied strain, indicative of a low critical resolved shear stress when subjected to axial extension and lateral compression, and to persist up to a strain $e_3 = 0.2$. As mentioned earlier, the system undergoing "fast" deformation then experiences a cavitation event. However, the system undergoing "slow" deformation exhibits a drop in crystallinity beginning as early as $e_3 = 0.1$ and continuing up to $e_3 = 0.3$. At this point, a reconstruction of the crystal domain occurs that re-establishes the lower energy {201}-oriented crystal−amorphous interface in concert with a twin boundary within the crystal phase and some degree of recrystallization. It thus appears that the yield and plastic flow that occurs in this system are associated primarily with melting and recrystallization.

Evolutions of Entanglements. We applied Kröger's Z algorithm[68] to characterize the entanglement network of the entire semicrystalline system, both in the undeformed state and as it undergoes deformation. In the undeformed state, N_e is 132 ± 7. Correcting for the volume fraction of the crystalline domain, in which we assume there are no entanglements, we obtain an entanglement density for the noncrystalline domain of 0.64 ± 0.03 nm^{-3}. This entanglement density compares with a simulated melt value of 0.53 nm^{-3}, or $N_e = 60$, for a bulk amorphous polyethylene at 450 K obtained by the same algorithm;[77] this latter value is in very good agreement with the experimental value ($N_e = 59$) at 413 K, based on SANS and the relation $G_N = \rho k_B T/M_e = \rho k_B T/m_0 N_e$.[78] This suggests that the interlamellar phase in semicrystalline polyethylene is more entangled than the amorphous polyethylene melt, based solely on equilibrium considerations. However, the origin of this increased entanglement density remains a topic for further investigation. We speculate that, because the interlamellar phase in semicrystalline polyethylene is confined between crystallites and a substantial number of loops is required to satisfy the density requirements, these topological differences are responsible for the increase in entanglement density.

There are two different points of view that are commonly used to explain the relation between crystallization and entanglement density in semicrystalline polymers. These differ in their understanding of the fate of entanglements on the time scale of the crystallization process. In the point of view proposed by Flory and Yoon,[76] it is assumed that macromolecules in the melt cannot disentangle on the time scale required for crystallization; that is, the disengagement time is longer than the inverse of the crystallization rate. In this case, entanglements should be conserved during crystallization, and they are segregated into the noncrystalline domain as crystallization proceeds, thereby implying a higher entanglement density in the noncrystalline domain as the volume fraction of crystallinity increases.[76] The second point of view, suggested by Hoffman and Miller to be applicable in regimes I and II of surface nucleation theory for crystal growth kinetics, where crystallization is slowest, asserts that long-range diffusion of macromolecules from the bulk to the crystal growth front is required for crystallization to proceed.[79] In this case, entanglements are eliminated as crystallization proceeds; whether the entanglement density in the remaining noncrystalline fraction is a constant of the crystallization process or not is unclear. On the basis of the concept of "forced reptation", Hoffman argues that a chains can be extracted from their entanglements with other chains and "reeled in" at a rate on the order of 10^{-3} cm/s, which is sufficient to accommodate growth rates (on the order of 10^{-5}−10^{-7} cm/s) typical for regimes I and II (cf. Figure 8 of ref 79).

Figure 14 displays the evolution of N_e during several deformation simulations. Because melting and recrystallization may occur during deformation, the volume fractions of crystalline and amorphous domains vary during the course of a simulation, whereas the Z-code as provided[80] does not distinguish between such internal heterogeneities; for this reason, we report N_e as reported by the Z code for the entire simulation (including both crystalline and noncrystalline domains) and assume for purposes of discussion that this includes contributions both from segments between entanglements in the noncrystalline domain and from segments comprising chain stems within an entanglement-free crystalline domain. With this picture in mind, it is evident that if the total number of entanglements in the simulation were conserved, then N_e would remain unchanged, on average, during deformation and melting/recrystallization; N_e depends only on the number of entanglements, the number of sites in the system, and the average polymer chain length, the latter two being conserved by construction. Instead, during the slow, volume-conserving deformation, N_e decreases from about 130 to about 95 between $0 < e_3 < 0.3$, and then it increases slightly; this is consistent with the variation in crystallinity (cf. Figure 13), indicating that as the crystallinity decreases, additional entanglements are created (presumably, in the noncrystalline domain). By contrast, during the fast deformation with fixed lateral dimension, there is no remarkable change in N_e, also consistent with the relatively constant crystallinity observed in that simulation. During the slow deformation with fixed lateral dimension, N_e decreases steeply from 130 to 95 between $0 < e_3 < 0.1$ and then declines more gradually. These changes in N_e correlate well with the changes in crystallinity shown in Figures 6 and 13. Thus, our results suggest that entanglements are created or eliminated readily in response to the production (melting) or removal

(recrystallization) of amorphous material as a consequence of tensile deformation occurring on the time scale of $1/\dot{e}_3 \sim 10$ ns, for the molecular weight of polyethylene (M_n = 13 100 g/mol) simulated here.

CONCLUSION

Using IMC and SM molecular dynamics simulations, we have simulated the plastic deformation of a model of semicrystalline polyethylene. In order to capture the contribution of the crystalline domain to yield and plasticity, it is necessary to thermalize the crystal domain as well as the noncrystalline domain, a feature that is missing in the IMC simulations. The elastic modulus is almost independent of the deformation rate, whereas the stress and strain at yield are quite sensitive to both mode of deformation and deformation rate. This difference can be traced to the different yield mechanisms that are operative in these cases. In the deformation at constant volume, rotation of the chains within the ordered crystal domains is observed, indicative of crystallographic slip. This mechanism is not found in the case of tensile strain deformation with fixed lateral dimensions. In particular, in the slow deformation at constant volume, the plastic flow takes place in concert with melting and recrystallization at the crystal–amorphous interfaces. For the other deformation simulations, yield occurs through cavitation. Employing Kröger's Z algorithm, we found that the entanglement length, and hence the total number of entanglements, of semicrystalline polyethylene correlates with the volume fraction of noncrystalline material. We believe that the mechanisms identified in molecular simulations of the type reported here can be used to inform micromechanical models, such at that reported by Lee et al.,[81] to describe large plastic deformation of a complex (e.g., spherulitic) semicrystalline morphology. Specifically, the important mechanisms of response and associated constitutive relations for the representative semicrystalline element can be identified and parametrized, while respecting the detailed molecular nature and topological constraints of the material under consideration.

AUTHOR INFORMATION

Corresponding Author

*E-mail: rutledge@mit.edu.

Present Addresses

†Samsung SDI Co., Ltd., Yongin-si, Gyeonggi-do 446-577, Korea.

ACKNOWLEDGMENT

Financial support of this work from ExxonMobil Research and Engineering Co. is gratefully acknowledged.

REFERENCES

(1) Flory, P. J.; Yoon, D. Y.; Dill, K. A. *Macromolecules* **1984**, *17*, 862–868.
(2) Mandelkern, L. *Macromol. Chem.* **1992**, *3*, 347.
(3) Baker, A. M. E.; Windle, A. H. *Polymer* **2001**, *42*, 667–680.
(4) Keller, A. *Philos. Mag.* **1957**, *2*, 1171.
(5) Fisher, E. W. *Z. Naturforsch., A* **1957**, *12*, 753.
(6) Till, P. H. *J. Polym. Sci.* **1957**, *24*, 301–306.
(7) Bassett, D. C. *Philos. Mag.* **1964**, *10*, 595.
(8) Strobl, G. R.; Hagedorn, W. *J. Polym. Sci., Polym. Phys. Ed.* **1978**, *16*, 1181–1193.
(9) Glotin, M.; Mandelkern, L. *Colloid Polym. Sci.* **1982**, *260*, 182–192.
(10) Axelson, D. E.; Mandelkern, L.; Popli, R.; Mathieu, P. *J. Polym. Sci., Polym. Phys. Ed.* **1983**, *21*, 2319–2335.
(11) Kitamaru, R.; Horii, F.; Hyon, S. H. *J. Polym. Sci., Polym. Phys. Ed.* **1977**, *15*, 821–836.
(12) Eckman, R. R.; Henrichs, P. M.; Peacock, A. J. *Macromolecules* **1997**, *30*, 2474–2481.
(13) Goderis, B.; Reynaers, H.; Koch, M. H. J.; Mathot, V. B. F. *J. Polym. Sci., Part B: Polym. Phys.* **1999**, *37*, 1715–1738.
(14) Schelten, J.; Ballard, D. G. H.; Wignall, G. D.; Longman, G. W.; Schmatz, W. *Polymer* **1976**, *17*, 751–757.
(15) Summerfield, G. C.; King, J. S.; Ullman, R. *J. Appl. Crystallogr.* **1978**, *11*, 548–551.
(16) Lustiger, A.; Lotz, B.; Duff, T. S. *J. Polym. Sci., Part B: Polym. Phys.* **1989**, *27*, 561–579.
(17) DiCorleto, J. A.; Bassett, D. C. *Polymer* **1990**, *31*, 1971–1977.
(18) Flory, P. J. *J. Am. Chem. Soc.* **1962**, *84*, 2857–2867.
(19) Yoon, D. Y.; Flory, P. *J. Faraday Discuss. Chem. Soc.* **1979**, *68*, 288–296.
(20) Yoon, D. Y. *J. Appl. Crystallogr.* **1978**, *11*, 531–535.
(21) Schmidt-Rohr, K.; Spiess, H. W. *Macromolecules* **1991**, *24*, 5288–5293.
(22) Reneker, D. H.; Mazur, J. *Polymer* **1983**, *23*, 401–412.
(23) Boyd, R. H. *Polymer* **1985**, *26*, 1123–1133.
(24) Galeski, A.; Bartczak, Z.; Argon, A. S.; Cohen, R. E. *Macromolecules* **1992**, *25*, 5705–5718.
(25) Hay, I. L.; Keller, A. *Kolloid Z. Z. Polym.* **1965**, *204*, 43.
(26) Young, R. J.; Bowden, P. B.; Ritchie, J. M.; Rider, J. G. *J. Mater. Sci.* **1973**, *8*, 23–36.
(27) Cowking, A.; Rider, J. G. *J. Mater. Sci.* **1969**, *4*, 1051.
(28) Wu, W.; Argon, A. S.; Turner, A. P. L. *J. Polym. Sci., Polym. Phys. Ed.* **1972**, *10*, 2397–2407.
(29) Frank, F. C.; Keller, A.; O'Conner, A. *Philos. Mag.* **1958**, *3*, 64.
(30) Bevis, M.; Crellin, E. B. *Polymer* **1971**, *12*, 666–684.
(31) Allan, P.; Crellin, E. B.; Bevis, M. *Philos. Mag.* **1973**, *27*, 127.
(32) Hay, I. L.; Keller, A. *J. Polym. Sci., Part C* **1970**, *30*, 289.
(33) Tanaka, K.; Seto, T.; Hara, T. *J. Phys. Soc. Jpn.* **1962**, *17*, 873.
(34) Kiho, H.; Peterlin, A.; Geil, P. H. *J. Appl. Phys.* **1964**, *35*, 1599.
(35) Galeski, A. *Prog. Polym. Sci.* **2003**, *28*, 1643–1699.
(36) Seguela, R. *J. Polym. Sci., Part B: Polym. Phys.* **2005**, *43*, 1729–1748.
(37) Bartczak, Z. *Macromolecules* **2005**, *38*, 7702–7713.
(38) Cheng, J. J.; Alvarado-Contreras, J. A.; Polak, M. A.; Penlidis, A. *J. Eng. Mater. Technol.* **2010**, *132*, 011026.
(39) Balijepalli, S.; Rutledge, G. C. *J. Chem. Phys.* **1998**, *109*, 6523–6526.
(40) Gautam, S.; Balijepalli, S.; Rutledge, G. C. *Macromolecules* **2000**, *33*, 9136–9145.
(41) Rutledge, G. C. *J. Mater. Sci., B* **2002**, *B41*, 909–922.
(42) Balijepalli, S.; Rutledge, G. C. *Comput. Theor. Polym. Sci.* **2000**, *10*, 103–113.
(43) in 't Veld, P. J.; Rutledge, G. C. *Macromolecules* **2003**, *36*, 7358–7365.
(44) Hütter, M.; in 't Veld, P. J.; Rutledge, G. C. *Polymer* **2006**, *47*, 5494–5504.
(45) in 't Veld, P. J.; Hütter, M.; Rutledge, G. C. *Macromolecules* **2006**, *39*, 439–447.
(46) Kuppa, V.; in 't Veld, P. J.; Rutledge, G. C. *Macromolecules* **2007**, *40*, 5187–5195; *Erratum* **2008**, *41*, 1896.
(47) Paul, W.; Yoon, D. Y.; Smith, G. D. *J. Chem. Phys.* **1995**, *103*, 1702–1709.
(48) Bolton, K.; Bosio, S. B. M.; Hase, W. L.; Schneider, W. F.; Hass, K. C. *J. Phys. Chem. B* **1999**, *103*, 3885–3895.
(49) Yi, P.; Rutledge, G. C. *J. Chem. Phys.* **2009**, *131*, 134902–134912.
(50) Waheed, N.; Lavine, M. S.; Rutledge, G. C. *J. Chem. Phys.* **2002**, *116*, 2301–2309.

(51) Ko, M. J.; Waheed, N.; Lavine, M. S.; Rutledge, G. C. *J. Chem. Phys.* **2004**, *121*, 2823–2832.
(52) Bassett, D. C.; Hodge, A. M. *Proc. R. Soc. London, A* **1981**, *377*, 25.
(53) Chui, C.; Boyce, M. C. *Macromolecules* **1999**, *32*, 3795–3808.
(54) Li, J.; Mulder, T.; Vorselaars, B.; Lyulin, A. V.; Michels, M. A. J. *Macromolecules* **2006**, *39*, 7774–7782.
(55) Mulder, T.; Li, J.; Lyulin, A. V.; Michels, M. A. J. *Macromol. Theory Simul.* **2007**, *16*, 348–358.
(56) Martyna, G. J.; Tuckerman, M. E.; Klein, M. L. *J. Chem. Phys.* **1992**, *97*, 2635–2643.
(57) Martyna, G. J.; Tobias, D. J.; Klein, M. L. *J. Chem. Phys.* **1994**, *101*, 4177–4189.
(58) Irving, J. H.; Kirkwood, J. G. *J. Chem. Phys.* **1950**, *18*, 817–829.
(59) Varnik, F.; Baschnagel, J.; Binder, K. *J. Chem. Phys.* **2000**, *113*, 4444–4453.
(60) Martyna, G. J.; Tuckerman, M. E.; Tobias, D. J.; Klein, M. L. *Mol. Phys.* **1996**, *87*, 1117–1157.
(61) Tuckerman, M. E.; Martyna, G. J.; Burne, B. J. *J. Phys. Chem.* **1992**, *97*, 1990–2001.
(62) Capaldi, F. M.; Boyce, M. C.; Rutledge, G. C. *Phys. Rev. Lett.* **2002**, *89*, 175505.
(63) Capaldi, F. M.; Boyce, M. C.; Rutledge, G. C. *Polymer* **2004**, *45*, 1391–1399.
(64) Pawlak, A. *Polymer* **2007**, *48*, 1397–1409.
(65) Wu, W.; Wignal, G. D.; Mandelkern, L. *Polymer* **1992**, *33*, 4137–4140.
(66) Koerner, H.; Liu, W.; Alexander, M.; Mirau, P.; Dowty, H.; Vaia, R. A. *Polymer* **2005**, *46*, 4405–4420.
(67) Everaers, R.; Sukumaran, S. K.; Grest, G. S.; Svaneborg, C.; Sivasubramanian, A.; Kremer, K. *Science* **2004**, *303*, 823–826.
(68) Kröger, M. *Comput. Phys. Commun.* **2005**, *168*, 209–232.
(69) Shanbhag, S.; Kröger, M. *Macromolecules* **2007**, *40*, 2897–2903.
(70) Tzoumanekas, C.; Theodorou, D. N. *Macromolecules* **2006**, *39*, 4592–4604.
(71) Crist., B.; Fisher, C. J.; Howard, P. R. *Macromolecules* **1989**, *22*, 1709–1718.
(72) Brooks, N. W. J.; Mukhtar, M. *Polymer* **2000**, *41*, 1475–1480.
(73) Gao, J.; Weiner, J. H. *Science* **1994**, *266*, 748–752.
(74) Gao, J.; Weiner, J. H. *J. Chem. Phys.* **1992**, *97*, 8698–8704.
(75) Gao, J.; Weiner, J. H. *Macromolecules* **1994**, *27*, 1201–1209.
(76) Flory, P. F.; Yoon, D. Y. *Nature* **1978**, *272*, 226–229.
(77) Foteinopoulou, K.; Karayiannis, N. C.; Mavrantzas, V. G.; Kröger, M. *Macromolecules* **2006**, *39*, 4207–4216.
(78) Fetters, L. J.; Lohse, D. J.; Richter, D.; Witten, T. A.; Zirkel, A. *Macromolecules* **1994**, *27*, 4639–4647.
(79) Hoffman, J. D.; Miller, R. L. *Polymer* **1997**, *38*, 3151–3212.
(80) http://www.complexfluids.ethz.ch/cgi-bin/mk.
(81) Lee, B. J.; Argon, A. S.; Parks, D. M.; Ahzi, S.; Bartczak, Z. *Polymer* **1993**, *34*, 3555–3575.